Research Article

Angewandte International Edition Chemie
www.angewandte.org

How to cite: *Angew. Chem. Int. Ed.* **2025**, *64*, e202418925
doi.org/10.1002/anie.202418925

Nanozymes **Hot Paper**

Topotactic Transformation in Fe_3O_4 Induces Spontaneous Growth of Compositionally Diverse Nanostructures

*Faheem Muhammad[+], Xiwen Chen[+], Qi Sun, Yuting Wang, Dongze Mo, Yuyang Li, Leiying Miao, and Hui Wei**

Abstract: Topotactic transformation is an emerging strategy for synthesizing materials with exotic functional properties. In this report, instead of producing new crystals with related structures, we exploited the topotactic transformation phenomenon to spontaneously produce compositionally diverse nanostructures on the transforming substrate. The surface of magnetite nanoparticles (Fe_3O_4 NPs) is topotactically transformed into maghemite (γ-Fe_2O_3). Benefiting from such oxidation susceptibility of ultrasmall Fe_3O_4 NPs, we achieved spontaneous growth of metals (Ag, Au, Pt, and Pd), a non-metal (Se), and a metal oxide (MnO_2) based nanostructures onto the surface of Fe_3O_4. No spontaneous growth of nanostructures was observed when the oxidized Fe_3O_4 NPs were tested, likely due to the loss of the Fe^{2+}-associated mobile electrons. The obtained nanostructures displayed appreciable antioxidant activities, which we utilized to effectively treat inflammation in the intestines. It is anticipated that this synthetic route, based on topotactic transformation, represents a significant advancement in synthesizing various chemically diverse hetero-nanostructures.

Introduction

Transition metal oxides (TMOs) have attracted significant attention because of their captivating physiochemical properties. Low cost, ease of fabrication, and eco-friendliness further elevate their technological significance, making them suitable for a wide range of practical applications across different domains, including catalysis, magnetic recording, photovoltaics, gas storage, sensors, medicine, environmental remediation, optoelectronic devices, energy storage, and conversion.[1] Among many valuable TMOs, the mixed-valent Fe_3O_4 is one of the most extensively studied materials. It has a face-centered cubic inverse spinel structure, consisting of Fe^{2+} and Fe^{3+} ions. In this structure, ferrous ions occupy half of the octahedral sites, while ferric ions are evenly distributed between the tetrahedral (A) and octahedral (B) sites.[2] Unlike the poor intrinsic electrical conductivity observed in other TMOs, Fe_3O_4 also exhibits fairly high electrical conductivity ($\sim 2\times 10^4\ \Omega^{-1}m^{-1}$) like a poor metal. The conductivity is attributed to the thermally activated polaronic hopping of Fermi surface electrons between Fe^{2+} and Fe^{3+} at equivalent B sites.[3] In TMOs, oxygen stoichiometry greatly influences the physiochemical properties; any variation in oxygen content in Fe_3O_4 understandably alters its electrochemical properties.[4] At near room temperature, Fe_3O_4 undergoes slow oxidation, and the rate of oxidation increases with O_2 fugacity and/or temperature, resulting in the reduction of Fe^{2+}/Fe^{3+} ratio from 0.5 in stoichiometric magnetite to 0 in maghemite (γ-Fe_2O_3).[5] Gallagher et al. explained the low-temperature oxidation phenomenon in Fe_3O_4 by proposing a diffusion model wherein the Fe^{2+} ions diffuse outward. They determined the distribution of Fe^{2+} across magnetite particles after various degrees of oxidation.[6] In simpler terms, during oxidation, Fe^{2+} ions migrate towards the surface, driven by the concentration gradient, where they are transformed to Fe^{3+}. These Fe^{3+} ions then coordinate with adsorbed oxygen (ionized by electrons released during the oxidation of Fe^{2+}), forming a maghemite layer with octahedral iron vacancies (eq. 1). The outward migration of Fe^{2+} is favored over the inward movement of oxygen atoms due to the smaller ionic radius (0.64 and 0.76 Å for Fe^{3+} and Fe^{2+} respectively) relative to far too large oxygen (1.40 Å). Sidhu et al. also corroborated the oxidation and diffusion model, whereas Yuan et al. recently demonstrated that the surface oxidized magnetite has a strained and defective structure, which

---

[*] F. Muhammad,[+] X. Chen,[+] Q. Sun, Y. Wang, D. Mo, Prof. Dr. H. Wei
Department of Biomedical Engineering, College of Engineering and Applied Sciences, Nanjing National Laboratory of Microstructures, Jiangsu Key Laboratory of Artificial Functional Materials, Nanjing University, Nanjing, Jiangsu 210023, China
E-mail: weihui@nju.edu.cn

F. Muhammad[+]
Guangdong Key Laboratory of Biomedical Measurements and Ultrasound Imaging, School of Biomedical Engineering, Shenzhen University Medical School, Shenzhen University, Shenzhen 518060, China

Y. Li, L. Miao
Department of Cariology and Endodontics, Nanjing Stomatological Hospital, Medical School of Nanjing University, Nanjing, 210008, China

Prof. Dr. H. Wei
State Key Laboratory of Analytical Chemistry for Life Science, School of Chemistry and Chemical Engineering, Chemistry and Biomedicine Innovation Centre (ChemBIC), ChemBioMed Interdisciplinary Research Centre at Nanjing University, Nanjing University, Nanjing, Jiangsu 210023, China

[+] These authors contributed equally to this work.

enhances its reactivity in an aqueous environment.[7] The migration of Fe^{2+} (or in other words Fe^{3+} and electron) in Fe_3O_4 NPs along with its defective structure offers us the opportunity to use this topotactically transforming reactive Fe_3O_4 for some useful purposes.

$$Fe_{16}(III)Fe_8(II)O_{32} \rightarrow Fe_{21.3}(III)O_{32} + 8e^- \quad (1)$$

Recently, there have been few reports on using reactive metal oxides for the spontaneous growth of metal NPs via oxygen vacancy-mediated or galvanic replacement reactions.[8] However, the topotactic transformation phenomenon for the spontaneous growth of multiple and chemically diverse nanostructures has been rarely documented. In this study, we have spontaneously grown different metals, non-metal, and metal oxide nanostructures on the surface of topotactically transforming Fe_3O_4 nanospheres. To highlight the distinctions of our study from the previously reported metal oxide-based spontaneous growth strategies, a table is created (Table S1). The excellent biocatalytic activities of the resulting nanostructures were subsequently utilized in treating intestinal inflammation.[9] Of the Fe_3O_4-based heterostructures, Pt-, Pd-, Ag-, Se- and MnO_2-containing nanostructures exhibited high efficacy in relieving the inflammatory condition owing to their superior antioxidant activities (superoxide dismutase (SOD) and catalase (CAT) like) and marked downregulation of pro-inflammatory biomarkers along with an upregulation of anti-inflammatory cytokines.

Results and Discussion

Magnetite NPs with controllable sizes and shapes are typically synthesized through the thermal decomposition of organometallic and coordination compounds in nonpolar solvents. The resulting product is stabilized by hydrophobic, nondegradable ligands. Although several ligand-exchange methods have been developed to make them hydrophilic, those procedures could lead to the oxidation of the Fe_3O_4 surfaces. As we intended to use freshly prepared (non-oxidized) Fe_3O_4, therefore we sought a method that could produce high-quality, water-dispersible Fe_3O_4 in a single step. In this study, uniform nanospheres of Fe_3O_4 composed of self-assembled ultrasmall NPs were prepared.[10] The use of multidentate sodium citrate during the synthesis ensured not only a uniform and non-aggregated Fe_3O_4 product (suitable for biomedical applications) but also the surface-bound COOH groups on Fe_3O_4. The COOH groups served as anchoring points for the attachment of oxidative metal salts during the spontaneous growth process of various nanostructures. The stoichiometry of Fe_3O_4 significantly influences its electrochemical properties, meaning that any noticeable change in composition can impact its conductivity and redox potential. To investigate this, we treated freshly prepared Fe_3O_4 under various oxidizing conditions. The aqueous solutions of Fe_3O_4 were aged at 37 °C for different durations (1, 3, and 5 days), and one solution was exposed to 50 mM H_2O_2. Additionally, the powder samples were thermally treated at 100 and 300 °C for 2 h. These treatments produced nonstoichiometric and fully oxidized γ-Fe_2O_3 products, as illustrated in the absorption spectra and digital photo provided in Figure S1. The obvious changes in the color of the solutions (from blackish to brownish color) and a progressive decrease in the near-IR absorption peak (due to charge transfer between Fe^{2+} and Fe^{3+}) implied the oxidation of mixed valent Fe_3O_4. Figure S2 indicates that the morphology and size of Fe_3O_4 nanospheres were not changed following the relatively harsh thermal treatment (300 °C, 2 h), showing nearly spherical-shaped and uniform nanospheres (~200 nm). The zeta potential measurement indicated a negative potential (−31.3 mV) of freshly prepared Fe_3O_4, whereas the positive value implied the decomposition of surface-bound carboxylate groups upon thermal treatment at 300 °C (Figure S3). Fourier transform infrared (FTIR) spectra similarly verified the presence of surface-bound multidentate carboxylate moieties (bands at 1652 and 1396 cm^{-1}) onto the surface of freshly prepared Fe_3O_4 (Figure S4). We also performed thermogravimetric analysis (TGA) to determine the organic content present in Fe_3O_4 nanospheres. Only a minimal amount of organic material (<5 %) was detected in the freshly prepared Fe_3O_4 sample, thus ruling out the role of organic material in the spontaneous growth of the nanostructures (Figure S5). The magnetic properties of freshly prepared and thermally treated (300 °C) Fe_3O_4 were determined using vibrating sample magnetometry (VSM). Both tested samples exhibited typical superparamagnetic behavior without a hysteresis loop at room temperature (300 K). The magnetization values (M_s) were found to be around 60 emu/g, as shown in Figure S6. These results validated the insensitivity of magnetic parameters to oxidation at lower temperatures because both magnetite and maghemite have spinel ferrite structures and are superparamagnetic. The X-ray diffraction pattern of the freshly prepared Fe_3O_4 showed relatively broad peaks indexed to diffraction from (220), (311), (400), (422), (511), and (440) planes of the magnetite cubic cell. Upon various oxidation treatments, no apparent difference between the two phases was detected, only a minor difference was identified in the sample treated at 300 °C in the form of a shift in (511) and (440) planes, as shown by the dashed lines in Figure S7.[11] The distinction between Fe_3O_4 and γ-Fe_2O_3 phases by their indexed planes is challenging because both are spinel phases of ferrites and share the same set of (hkl) planes. Additionally, the Fe_3O_4 nanospheres used in this study are composed of self-assembled small-sized particles (~5–10 nm), which produce broad and weak peaks, further complicating the differentiation among the various treated samples. X-ray photoelectron spectroscopy (XPS) provided insights into the composition and oxidation states of the treated Fe_3O_4 samples. The deconvoluted high-resolution XPS spectra of various oxidized Fe_3O_4 samples are presented in Figure S8a, revealing a gradual reduction in the intensities of peaks associated with Fe^{2+}, particularly in the Fe $2p_{3/2}$ region. Additionally, a more prominent satellite peak at approximately 719.0 eV was observed in the treated Fe_3O_4 samples (especially the sample treated at 300 °C), indicating the presence of the trivalent oxidation state of iron in γ-Fe_2O_3.[4b,12]

After investigating the oxidation susceptibility of Fe_3O_4, nearly stoichiometric Fe_3O_4 was tested as a redox-active substrate to spontaneously grow nanostructures. Under optimized conditions, when various oxidative metal salts were exposed to a freshly prepared aqueous solution of Fe_3O_4, a variety of nanostructures were readily deposited onto its surface (Figure 1b). These materials included noble metals (Ag, Au, Pt, and Pd), non-metal (Se) NPs, and metal oxide (MnO_2) nanosheets (digital photos in Figure S9). The characteristic features of surface plasmon resonance appeared in Ag- and Au-containing samples with relatively broad peaks at around 560 nm and 520 nm respectively. No

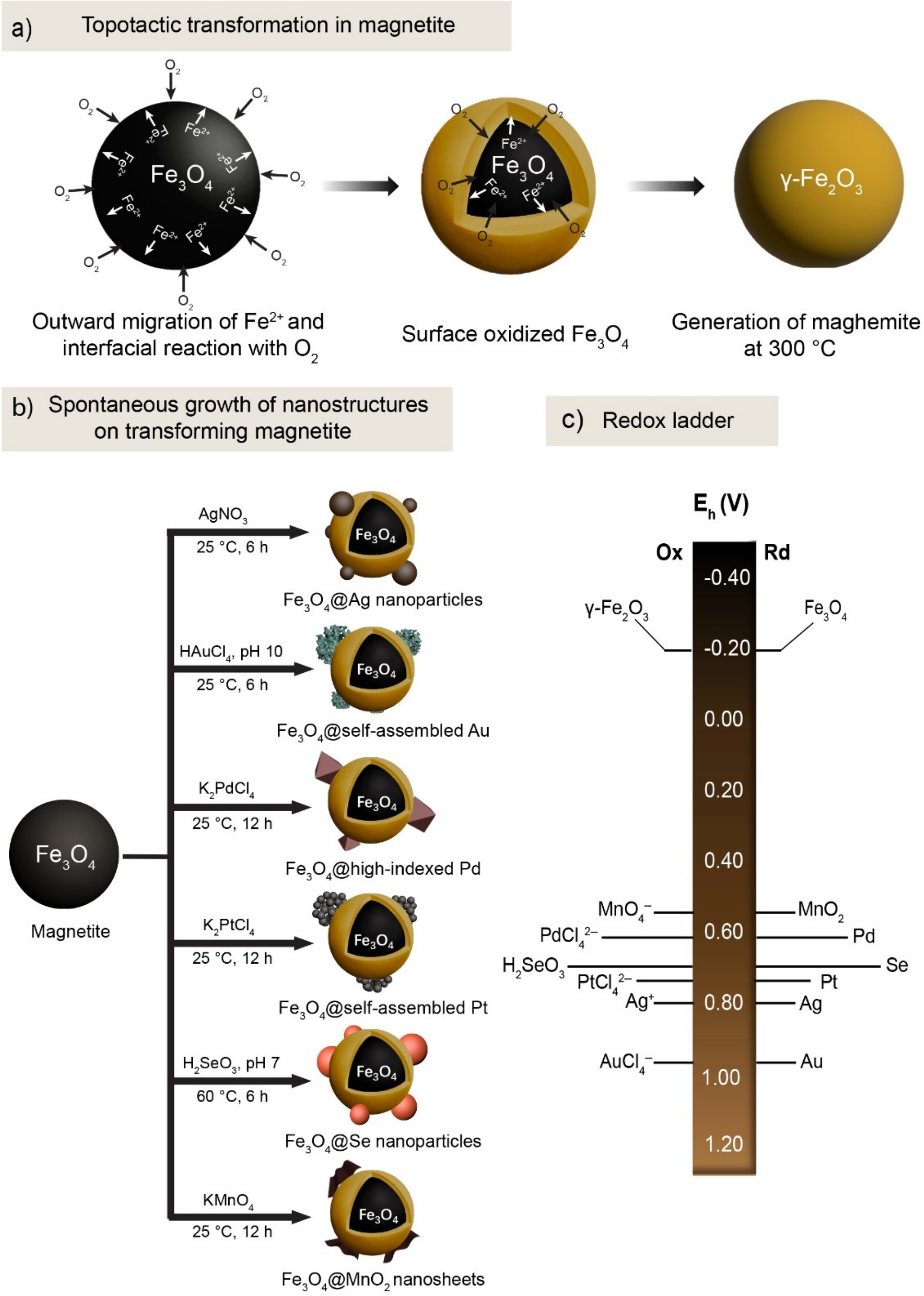

Figure 1. Scheme depicting the topotactic transformation in magnetite, synthetic conditions, and redox ladder for the spontaneous growth of different nanostructures on magnetite. (a) Schematic diagram indicating the topotactic transformation occurring in the magnetite crystal structure. (b) Schematic diagram showing the synthetic protocol used for the spontaneous growth of compositionally diverse nanostructures on the surface of freshly prepared Fe_3O_4. (c) Scheme of the redox ladder, showing the redox potentials of different oxidative metal salts.

obvious changes in UV spectra of other Fe_3O_4-based samples were observed, likely due to the more intense absorption behavior of the Fe_3O_4 substrate. The atomic ratio of Fe_3O_4 to the other six components in the spontaneously grown Fe_3O_4-based nanostructures was determined by inductively coupled plasma optical emission spectroscopy (ICP-OES). The amounts of Ag, Au, Pd, Pt, Se, and Mn were found to be 135.0, 108.3, 65.3, 88.9, 37.4, and 64.2 mg/g of Fe_3O_4, respectively.

Using scanning electron microscopy (SEM) and transmission electron microscopy (TEM), the size, morphology, and crystalline nature of different spontaneously generated nanostructures were analyzed. Marked differences in SEM and TEM images can be readily seen following the redox reactions of Fe_3O_4 with different oxidative precursors of metals, non-metal, and metal oxide. The spontaneous deposition of Ag NPs is quite visible in Figure 2a due to the Z-contrast and its crystalline large particle size (20–30 nm). SEM, low and high-resolution TEM (HRTEM) images show the self-assembled Au nanostructure spontaneously grown onto the surface of Fe_3O_4 (Figure 2b). Because of the highest positive reduction potential of $HAuCl_4$ relative to the other precursors, partially or completely oxidized Fe_3O_4 NPs were also exposed to the gold precursor to evaluate the spontaneous reduction process. Figure S10 shows the grown Au nanostructures, these results demonstrate the spontaneous generation of Au nanostructures on even nonstoichiometric Fe_3O_4 but at a somewhat lower yield compared to freshly prepared more stoichiometric Fe_3O_4. However, substantially oxidized Fe_3O_4 product (treated at 300 °C) failed to spontaneously produce Au whatsoever over 24 h, validating the influence of stoichiometry on the reducing power of Fe_3O_4. The samples were also analyzed by ICP-OES to determine the content of deposited Au. The amounts of Au were found to be 49.3, 47.5, 39.4, 37.8, and 35.6 mg/g of Fe_3O_4 in 1 d, 3 d, and 5 d, H_2O_2, and 100 °C samples, respectively. The Au growth kinetics was also studied over different periods by collecting the Fe_3O_4@Au products after 6, 24, 48, and 72 h. The ICP-OES analysis, as shown in Figure S11, revealed that most of the Au product was formed within 24 h, and no further appreciable growth of Au was detected in the next 48 h, implying that the redox-active surface of Fe_3O_4 was mainly involved in the spontaneous growth process. Once the surface of Fe_3O_4 is oxidized by the oxidative metal salts (or oxygen), further oxidation of the inner core of Fe_3O_4 is severely slowed down at room temperature, higher temperatures are then required to accelerate the outward migration of reactive Fe^{2+} ions. In another control experiment, instead of Fe_3O_4, two adjacent spinel metal oxides (i.e., Co_3O_4 and Mn_3O_4) were exposed to the gold precursor in the presence of sodium citrate at room temperature for 6 h. As shown in Figure S12, no spontaneous growth of Au on the surfaces of Co_3O_4 and Mn_3O_4 was observed, verifying the role of topotactic transformation (or oxidation vulnerability) in Fe_3O_4 to spontaneously produce nanostructures. Palladium was grown in the form of high-index faceted octahedra/truncated octahedra onto the surface of Fe_3O_4, without using any specialized synthetic conditions or structure-directing template, as shown in Figure 2c. The compositional maps of Pd, Fe, and O corroborated the successful growth of palladium nanostructure. Examination of the SEM and TEM images in Figure 2d reveals the appearance of additional self-assembled nanostructure with high contrast readily distinguishable from the Fe_3O_4 nanospheres, unambiguously verifying the growth of Pt. Interestingly, identical to the structure of Au, the self-assembled structured Pt was also generated without using any structure-directing agents. The elemental distribution mapping of the Pt nanostructure grown on Fe_3O_4 is also shown. It appears that platinum ions were likely reduced on the redox-active Fe_3O_4 nanospheres, progressively growing into self-assembled Pt nanostructures (approximately 50 nm in size). Due to ultrasmall size and low yield, spontaneously grown Se could not be seen in SEM analysis. However, TEM examination shows that the Fe_3O_4 core was surrounded by ultrasmall (~2 nm) Se NPs, the EDX analysis also verified the presence of Se (Figure 2e**)**. Sheet-like MnO_2 was spontaneously grown onto the surface of Fe_3O_4 after exposure to $KMnO_4$ solution. Well-defined 2D sheets of MnO_2 are visible on the surface of Fe_3O_4, forming a flower-like shell, as shown in Figure 2f.

Figure 3a shows the XRD patterns of Fe_3O_4 and the deposited nanostructures. After the redox reactions with various oxidative metal salts, in addition to the characteristic diffraction peaks of Fe_3O_4, additional peaks also appeared. We detected peaks corresponding to the (111) and (200) planes of metallic Ag, while the peaks at 38.3° and 44.8° were indexed to the face-centered cubic structure of Au. The XRD patterns of the Fe_3O_4@Pd samples confirmed the growth of Pd, peaks at 40.2°, 46.6°, and 68.3° were assigned to the (111), (200), and (220) interplanar spacings, respectively. Sharp and characteristic Pt-associated peaks were observed, whereas a weak and broad peak of Se NPs was noticed, likely due to the small size and low deposited content. No apparent peaks of MnO_2 were detected, likely due to the ultrathin nanosheet-like structure and poor crystallinity relative to Fe_3O_4 substrate. The matched JCPDS files of all the deposited nanostructures are shown with XRD results. Moreover, to find whether the crystal structure of Fe_3O_4 was transformed during the growth of nanostructures, we drew dashed lines to track the peak shift in (511) and (440) planes. However, no peak shift was detected, as the nanostructures were generated under very mild reaction conditions, utilizing the topotactically transforming surface of Fe_3O_4.

Using XPS analysis, the appearance of the characteristics binding energies in the high-resolution spectra of the Ag 3*d*, Pd 3*d*, Se 3*d*, Au 4*f*, Pt 4*f*, and Mn 2*p* regions indicated the successful spontaneous growth of diverse nanostructures (Figure 3b). The presence of metallic Ag NPs was confirmed by the representative peaks at 368.2 and 374.1 eV in the Ag 3*d* spectrum. For Fe_3O_4@Au, two peaks at 84.0 and 87.7 eV were assigned to Au $4f_{7/2}$ and Au $4f_{5/2}$, respectively. In the case of Fe_3O_4@Pt, the doublet of binding energies at 71.0 (Pt $4f_{7/2}$) and 74.4 eV (Pt $4f_{5/2}$) confirmed the presence of metallic Pt^0, while the deconvoluted spectrum also implied the existence of the PtO. The Se 3*d* peak was comprised of two components: $3d_{3/2}$ and $3d_{5/2}$, separated by 0.86 eV. The

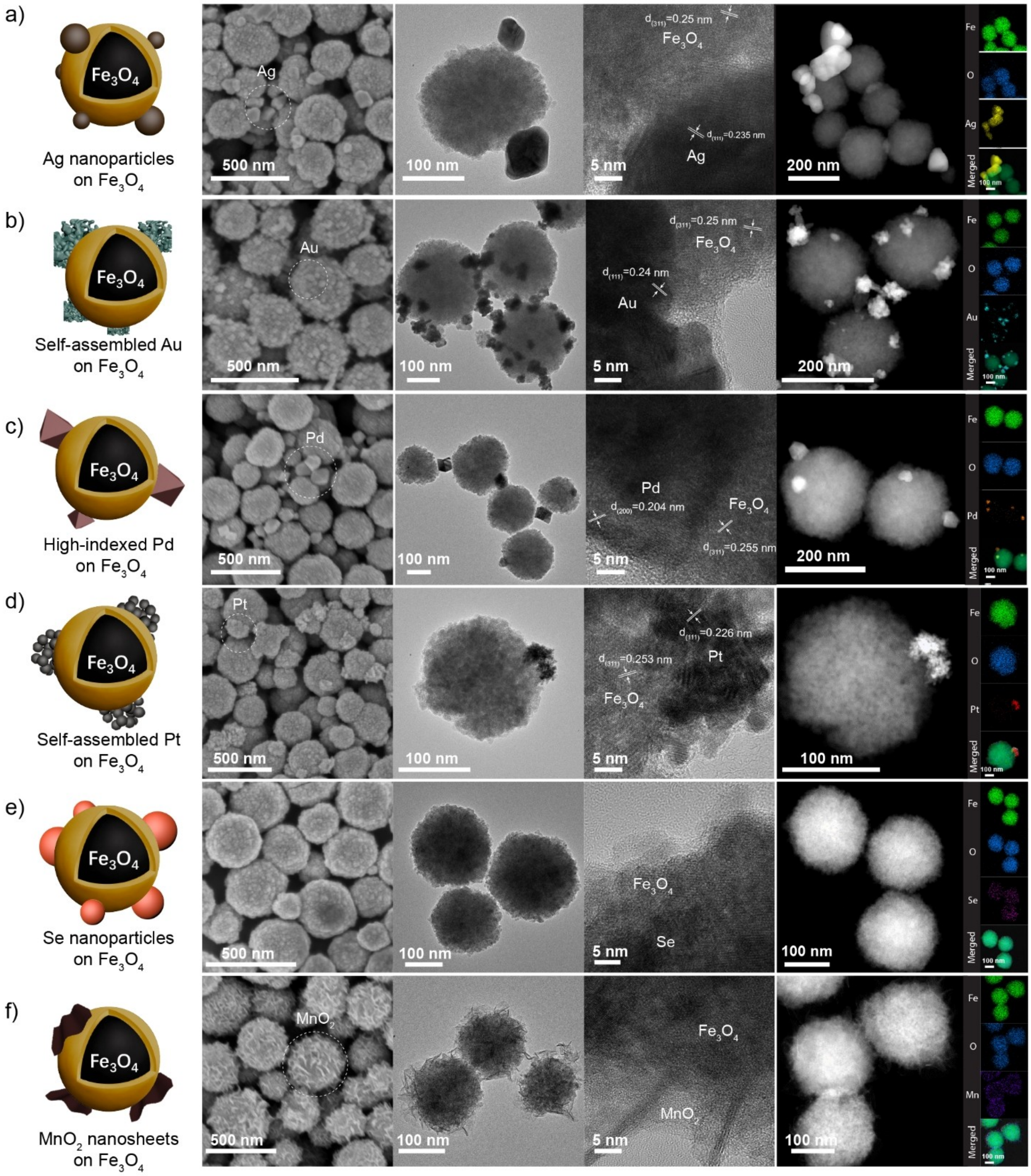

Figure 2. Structural and compositional analysis of spontaneously grown nanostructures on Fe_3O_4 by electron microscopy. (a–f) Schematic diagram, SEM, TEM, HRTEM, STEM, and elemental mapping images of Fe_3O_4@Ag, Fe_3O_4@Au, Fe_3O_4@Pd, Fe_3O_4@Pt, Fe_3O_4@Se, and Fe_3O_4@MnO_2 nanostructures.

binding energy at 55.1 eV ($3d_{5/2}$) confirmed the presence of metallic selenium, whereas the deconvoluted peak at approximately 57.7 eV implied the existence of an oxidized divalent component. The high-resolution Pd 3*d* spectrum revealed the presence of four peaks at 335.4, 340.7, 336.2, and 341.7 eV, corresponding to Pd^0 and Pd^{2+}, respectively. In the Mn 2*p* spectrum, two peaks appeared for Mn $2p_{1/2}$ and Mn $2p_{3/2}$ with binding energies of 653.7 and 642.4 eV, respectively. A deconvoluted analysis of these peaks indicated the presence of primarily Mn^{3+} and Mn^{4+}, signifying the formation of MnO_2.

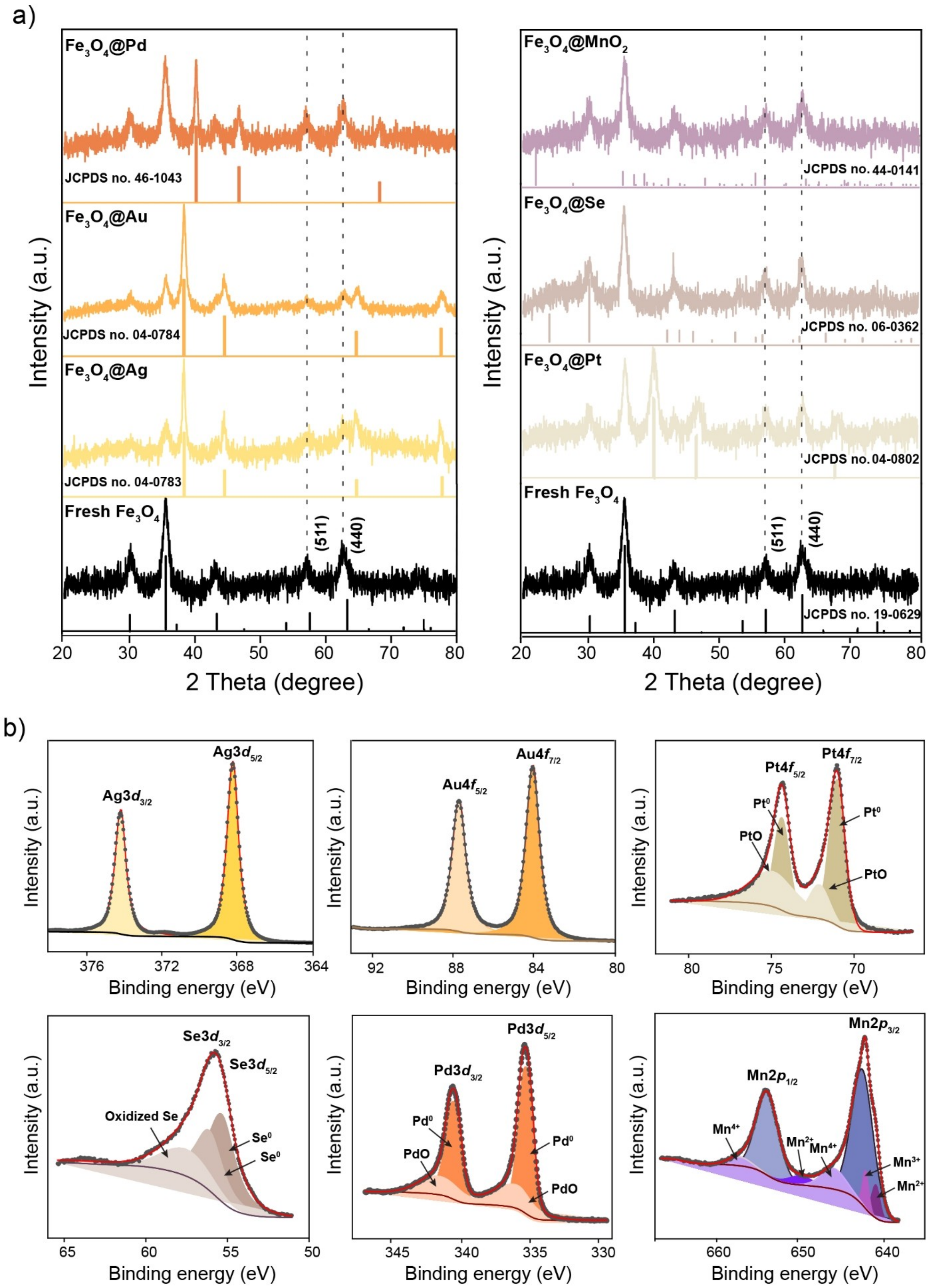

Figure 3. Compositional analysis of spontaneously grown Fe_3O_4-based nanostructures. (a) XRD diffraction patterns and (b) deconvoluted high-resolution XPS spectra of Fe_3O_4@Ag, Fe_3O_4@Au, Fe_3O_4@Pt, Fe_3O_4@Se, Fe_3O_4@Pd, Fe_3O_4@MnO_2, corroborating the spontaneous growth on topotactically transforming Fe_3O_4.

This spontaneous growth of multiple chemically diverse nanostructures on the surface of Fe_3O_4 can be attributed to its high conductivity and topotactic transformation process (oxidation susceptibility). The reduction potential of the Fe_3O_4 NPs is thermodynamically more negative (−0.2 V vs. NHE) compared to the redox potentials of the selected oxidative metal salts (i.e., +0.93, +0.80, +0.75, +0.74, +0.59, and +0.59 V vs. NHE for $AuCl_4^-$, Ag^+, $PtCl_4^{2-}$, H_2SeO_3, $PdCl_4^{2-}$, and MnO_4^-, respectively). The redox potentials of various couples are also shown as a redox ladder in Figure 1c.[13] When these oxidative metal salts are added to an aqueous solution of Fe_3O_4, heterogeneous interfacial redox reactions due to the outward migrating Fe^{2+} occur, leading to the spontaneous growth of various compositionally diverse nanostructures. In addition to redox potential, the growth of nanostructures also depends on the pH of the solution, temperature, and the properties of the selected metal salts. We optimized the reaction conditions, such as pH and temperature, in this study to obtain the desired nanostructures. The experimental details are described in the Supporting Information.

Magnetite has been extensively explored for various biological applications such as bioseparation, magnetic resonance imaging (MRI), cancer therapy, biosensing, and immunoassays due to its biocompatibility, high saturation magnetization, and low toxicity. Previous studies have also demonstrated that Fe_3O_4 acts as a reactive oxygen species (ROS) scavenger. More importantly, the nanostructures we spontaneously deposited on the surface of Fe_3O_4 exhibit more potent antioxidant capabilities, thereby motivating us to evaluate the antioxidant/anti-inflammatory activities of spontaneously produced nanostructures.[14] To evaluate the antioxidant activities, we first measured the SOD-like activity via the WST-1 kit. In this assay, the presence of nanostructures inhibited the formation of detectable formazan dye.

A noticeable quenching of superoxide radicals ($O_2^{\bullet-}$) was observed when various Fe_3O_4-based spontaneously grown nanostructures were exposed to reactive radicals. Specifically, Ag- and MnO_2-containing samples displayed excellent ROS scavenging abilities, 20 μg/ml of Fe_3O_4@Ag was found enough to quench 100 % of $O_2^{\bullet-}$, as shown in Figure 4a. The greater oxidation susceptibility of Ag (relative to other deposited metals) and the defective, ultrathin sheet-like structure of MnO_2 likely contributed to the enhanced quenching effects. Samples with Au, Pt, Pd, and Se also demonstrated $O_2^{\bullet-}$ scavenging activities. The treated Fe_3O_4 samples displayed poor performance due to their already oxidized and inactive surfaces.

The CAT-like activity of nanostructures was assessed by measuring the decomposition of H_2O_2 using a dissolved oxygen meter. Compared to fresh Fe_3O_4, the deposition of four components (Ag, Pd, Pt, and MnO_2) significantly enhanced the CAT-like activities by 44-, 28-, 44-, and 26-fold, respectively. (Figure 4b). The high CAT-like activities of these four materials have previously been reported both computationally and experimentally under neutral pH.[15] In contrast, the remaining samples, including Fe_3O_4, treated Fe_3O_4, Au, and Se, showed poor performance in catalyzing the decomposition of H_2O_2. This was primarily due to the relative stability of Au against H_2O_2 and the already oxidized, inactive surfaces of Se and Fe_3O_4 samples. Our findings demonstrated that even though the Fe_3O_4 substrate exhibited inferior CAT- and SOD-like activities, it induced the spontaneous growth of much more potent antioxidant nanostructures.

The preliminary higher biocatalytic activities provided us the impetus to investigate the cellular ROS scavenging and anti-inflammatory responses of these nanostructures. The cytotoxicity of Fe_3O_4-based antioxidants was first evaluated against RAW264.7 cells using a CCK-8 assay, the results substantiated the biocompatibility at therapeutic doses (Figure S13). The intracellular levels of ROS in both unstimulated and H_2O_2-stimulated RAW264.7 cells were measured using flow cytometry. A significant increase in ROS levels was observed in the cells treated with H_2O_2 (mean fluorescence of ROS increased by 3.37-fold). However, incubation with Fe_3O_4-based antioxidants (25 μg/mL) resulted in a significant reduction in the strong green fluorescence signals of 2′,7′-dichlorodihydrofluorescein diacetate (DCFH-DA). In the Fe_3O_4@Pd, Fe_3O_4@Ag, Fe_3O_4@Pt, and Fe_3O_4@MnO_2 treated groups, over 99 % of ROS induced by H_2O_2 were scavenged, demonstrating their highly effective ROS scavenging potential. The treated cells were also examined under a fluorescence microscope. A substantial decrease in green fluorescence was observed across all seven samples, including fresh Fe_3O_4, Fe_3O_4@Pd, and Fe_3O_4@Se. The quenching occurred despite these samples exhibiting low SOD- and CAT-like activities, suggesting that the specified concentration was high enough to scavenge intracellular ROS by even relatively weak antioxidants (Figures 4c and 4d). The anti-inflammatory effect of Fe_3O_4-based antioxidants was quantified via qPCR analysis. Following the LPS stimulation, the mRNA expressions of TNF-α, IL-1β, and IL-6 (pro-inflammatory factors) were significantly upregulated by 25-, 16-, and 68-fold, respectively, whereas the treatment with different Fe_3O_4-based antioxidants led to a marked decline in M1 markers. An obvious upregulation in the anti-inflammatory M2 markers (i.e., IL-10, TGF-β, and Arg-1) was noticed in Fe_3O_4@Ag, Fe_3O_4@Pd, Fe_3O_4@Pt, Fe_3O_4@Se, and Fe_3O_4@MnO_2 samples ($P < 0.001$), as shown in Figure 4e. The observed *in vitro* anti-inflammatory performance implies that Fe_3O_4-based antioxidants could significantly scavenge the intracellular ROS, promote macrophage M2 polarization, and thereby reduce cellular inflammatory conditions.

Inflammatory bowel disease (IBD) is a group of chronic, relapsing gastrointestinal disorders. There is increasing evidence that implicates a dysregulated immune system in the pathogenesis and progression of IBD. At the site of inflammation, an excessive amount of ROS is invariably produced by leukocytes and monocytes, leading to endothelial dysfunction and tissue injury. To counter the harmful impact of ROS, several antioxidant-based therapeutic strategies are being explored for the treatment of IBD. Given the satisfactory antioxidant and anti-inflammatory activities of Fe_3O_4-based nanostructures, we evaluated their potential therapeutic efficacy in ulcerative colitis (UC). Inflammation

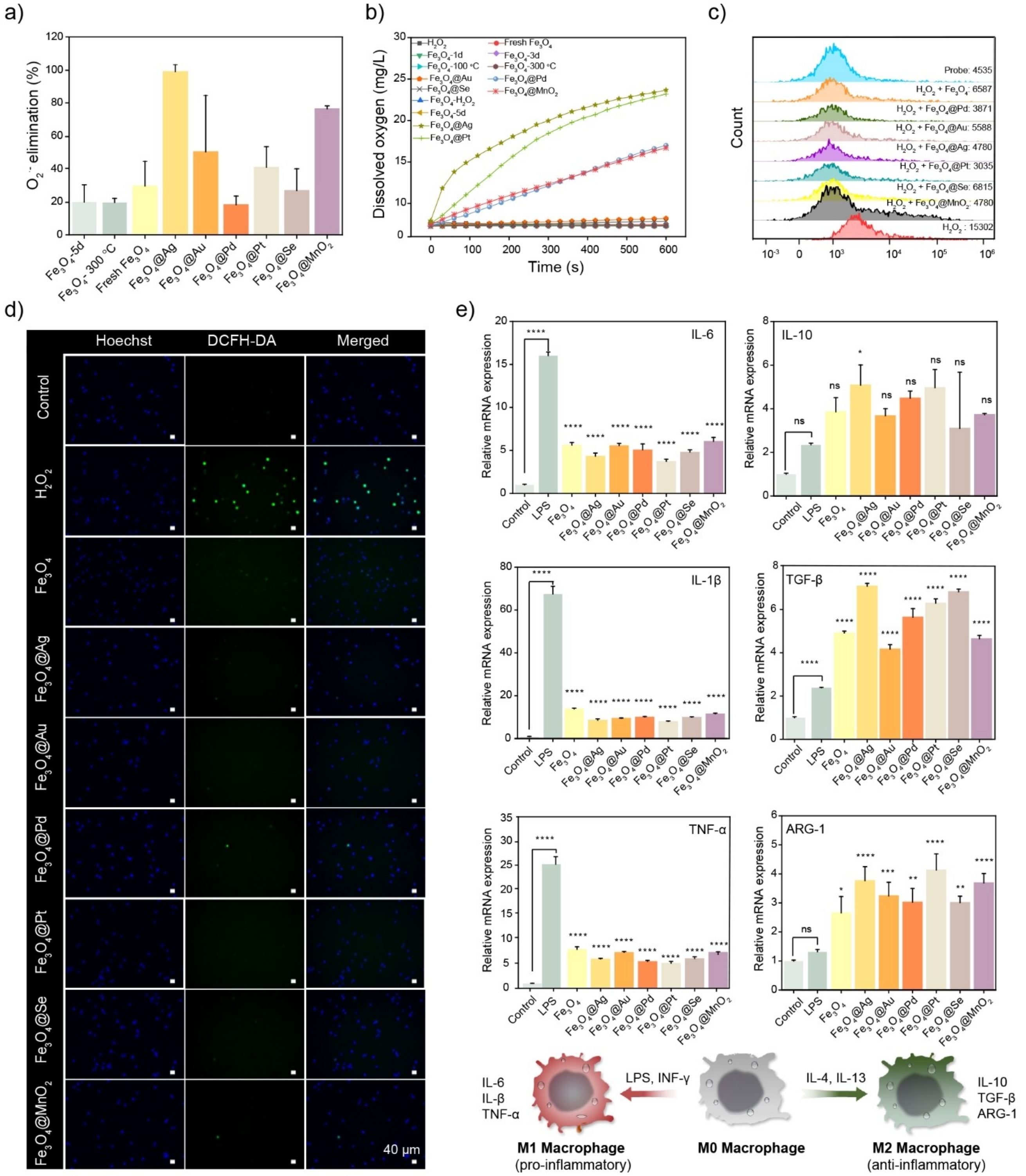

Figure 4. ROS scavenging and anti-inflammatory activities of Fe_3O_4-based nanostructures. (a and b) SOD- and CAT-like activities of compositionally diverse Fe_3O_4-based nanostructures. The Fe_3O_4 with 1 d, 3 d, 5 d, and 100 °C, 300 °C denote those samples, which underwent oxidation treatments. (c) Flow cytometry for the assessment of ROS scavenging in RAW 264.7 cells following the treatment with various Fe_3O_4-based nanostructures (25 μg/mL). (d) Fluorescent images indicate the ROS scavenging after treatment with tested nanostructures (DCFH-DA and Hoechst were used as ROS probe and nucleus dye respectively). (e) Anti-inflammatory effect of different Fe_3O_4-based nanostructures (12.5 μg/mL) on mRNA levels of pro-inflammatory (TNF-α, IL-1β, and IL-6) and anti-inflammatory (IL-10, TGF-β, and Arg-1) cytokines. Schematic representation illustrating the typical M1 and M2 polarization of macrophages and gene interference. Data are shown as means ± SD ($n=3$). Statistical analysis was performed using one-way ANOVA, specific P-values are shown in the source data.

in the bowel was triggered using dextran sulfate sodium (DSS), as illustrated in Figure 5a. After eight days of DSS administration, a significant loss in body weight (the average weight decreased by 9.4 % compared to the original average

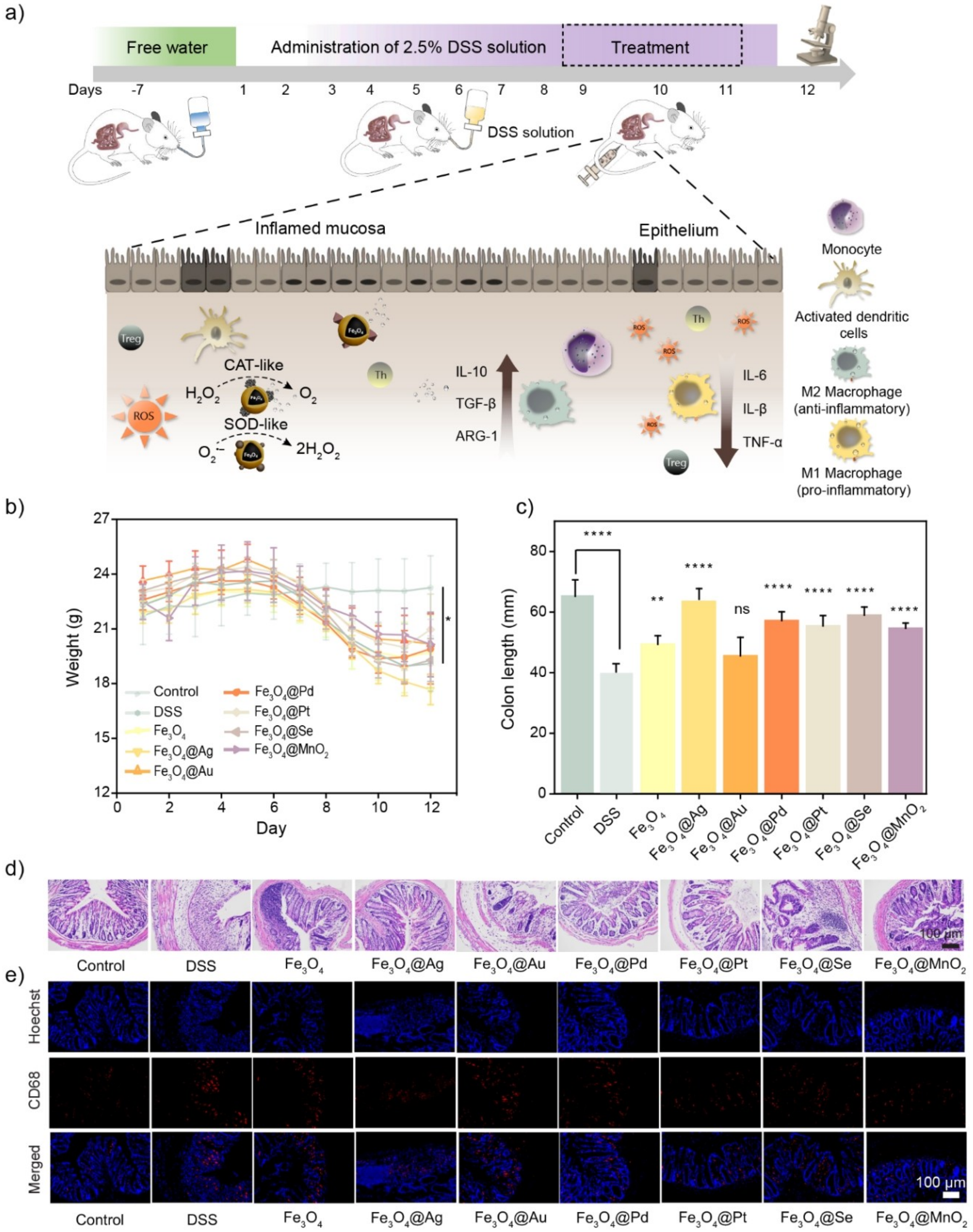

Figure 5. The study protocol and the evaluation of anti-inflammatory therapy in ulcerative colitis disease model. (a) Schematic diagram showing the protocol for induction of disease and the subsequent treatment using the antioxidant and anti-inflammatory activities of Fe_3O_4-based nanostructures. (b) Daily body weight was recorded while undergoing treatments with different Fe_3O_4-based antioxidants. (c) Statistical length of colon taken on day 12. (d) H&E-stained sections of colons following Fe_3O_4-based antioxidants treatment. (e) Representative images of immunofluorescence staining and quantification for CD68-positive immune cells. Data are shown as means ± SD ($n = 5$). Statistical analysis was performed using one-way ANOVA, specific *P*-values are shown in the source data.

weight) and shortening of colon lengths (from 65.68 ± 2.1 to 39.79 ± 6.4 mm) were noticed, implying the successful establishment of UC. Subsequently, as a treatment, different Fe_3O_4-based antioxidants were orally administered for three successive days, and the therapeutic efficacy was monitored by assessing the changes in body weight, colon length, and levels of immune cells, and analyzing the histologically stained colon sections. An obvious improvement in the body weights and apparent recovery in colon lengths to normal levels was observed (particularly in Fe_3O_4@Ag, Fe_3O_4@Pd, Fe_3O_4@Pt, Fe_3O_4@Se, and Fe_3O_4@MnO_2 samples, $P < 0.0001$), as shown in Figures 5b, 5c and S14. The relatively poor performance of Fe_3O_4 and Au-containing nanostructure was expected as they displayed low SOD- and CAT-like activities. To further confirm the therapeutic efficacy, hematoxylin and eosin (H&E) staining was carried out; the stained colon sections showed improved histological appearances in treated groups (Figure 5d). The tissues in treatment groups maintained normal morphology, particularly in the Fe_3O_4@Ag and Fe_3O_4@Pt groups, where the best tissue morphology was observed. No inflammatory cell aggregation, mucosal tissue detachment, shedding, or loss were noticed. Immunofluorescent staining was performed to evaluate the infiltration of macrophages. In DSS-induced mice, a higher level of macrophage infiltration was detected in the colon. In contrast, a considerable decline in the expression of CD68-positive immune cells was observed in the Fe_3O_4@Ag, Fe_3O_4@Pt, and Fe_3O_4@MnO_2 groups, demonstrating the anti-inflammatory effect of the developed nanostructures, as shown in Figure 5e. These results demonstrated that the *in vitro* antioxidant and anti-inflammatory activities of the Fe_3O_4-based nanostructures were translated well to the *in vivo* inflammation disease model. The *in vivo* biosafety of Fe_3O_4-based antioxidants was studied by examining the histopathology, H&E-stained sections of the heart, liver, spleen, lungs, and kidney demonstrated no appreciable differences from the control group (Figure S15).

Conclusions

Under ambient conditions, the surface of Fe_3O_4 NPs undergoes complex phase transitions; a gradual conversion of Fe_3O_4 into maghemite (γ-Fe_2O_3) phase has been widely reported. In this study, the oxidation vulnerability of ultrasmall redox-active Fe_3O_4 NPs was exploited to achieve the growth of compositionally diverse (Ag, Au, Pt, Pd, Se, and MnO_2) nanostructures onto the surface of Fe_3O_4, without using any additional reducing, structural directing and stabilizing agents. In terms of mechanism, the spontaneous growth process involved the reduction of oxidative metal salts at the surface of Fe_3O_4 by electrons released during the oxidation of structural Fe^{2+} atoms. We also found that magnetite stoichiometry ($x = Fe^{2+}/Fe^{3+}$) determines the reduction rates. No in situ spontaneous redox reactions were observed on completely oxidized Fe_3O_4 NPs, highlighting the importance of the availability of Fe^{2+}-associated mobile electrons to reduce the different oxidative metal salts. The antioxidant potential of the resulting materials was explored to treat inflammatory bowel disease. The therapeutic performance of Ag-, Pt-, Pd-, Se- and MnO_2-containing nanostructures was found to be satisfactory in providing relief in the disease model. The use of topotactic transformation in Fe_3O_4 to generate a range of compositionally diverse nanostructures represents a significant advancement in the field of material synthesis.

Acknowledgements

This work was supported by Jiangsu Provincial Key R&D Program-Social Development (BE2022836), National Key R&D Program of China (2019YFA0709200 and 2021YFF1200700), National Natural Science Foundation of China (22374071 and 11874199), PAPD Program, State Key Laboratory of Analytical Chemistry for Life Science (5431ZZXM2306), and Fundamental Research Funds for the Central Universities (202200325 and 021314380228). The writing was polished with the assistance of OpenAI.

Conflict of Interest

The authors declare no conflict of interest.

Data Availability Statement

The data that support the findings of this study are available from the corresponding author upon reasonable request.

Keywords: Antioxidants · Anti-inflammatory therapy · Magnetite · Reactive oxygen species · Topotactic transformation

---

[1] a) S. Yuan, X. Duan, J. Liu, Y. Ye, F. Lv, T. Liu, Q. Wang, X. Zhang, *Energy Storage Mater.* **2021**, *42*, 317–369; b) S. Fang, D. Bresser, S. Passerini, *Adv. Energy Mater.* **2020**, *10*, 1902485; c) B. Liu, J. Liu, *TrAC Trends Anal. Chem.* **2019**, *121*, 115690; d) X. Yu, T. J. Marks, A. Facchetti, *Nat. Mater.* **2016**, *15*, 383–396; e) H. Yoon, M. Choi, T.-W. Lim, H. Kwon, K. Ihm, J. K. Kim, S.-Y. Choi, J. Son, *Nat. Mater.* **2016**, *15*, 1113–1119; f) S.-I. Ohkoshi, A. Namai, M. Yoshikiyo, K. Imoto, K. Tamazaki, K. Matsuno, O. Inoue, T. Ide, K. Masada, M. Goto, T. Goto, T. Yoshida, T. Miyazaki, *Angew. Chem. Int. Ed.* **2016**, *55*, 11403–11406; g) D. Chen, C. Chen, Z. M. Baiyee, Z. Shao, F. Ciucci, *Chem. Rev.* **2015**, *115*, 9869–9921; h) I. Grinberg, D. V. West, M. Torres, G. Gou, D. M. Stein, L. Wu, G. Chen, E. M. Gallo, A. R. Akbashev, P. K. Davies, J. E. Spanier, A. M. Rappe, *Nature* **2013**, *503*, 509–512; i) J. Wang, J. B. Neaton, H. Zheng, V. Nagarajan, S. B. Ogale, B. Liu, D. Viehland, V. Vaithyanathan, D. G. Schlom, U. V. Waghmare, N. A. Spaldin, K. M. Rabe, M. Wuttig, R. Ramesh, *Science* **2003**, *299*, 1719–1722; j) M. Uehara, S. Mori, C. H. Chen, S. W. Cheong, *Nature* **1999**, *399*, 560–563.

[2] a) J. Baumgartner, A. Dey, P. H. H. Bomans, C. Le Coadou, P. Fratzl, N. A. J. M. Sommerdijk, D. Faivre, *Nat. Mater.* **2013**, *12*, 310–314; b) S. Laurent, D. Forge, M. Port, A. Roch, C. Robic, L. Vander Elst, R. N. Muller, *Chem. Rev.* **2008**, *108*, 2064–2110; c) S. Sun, H. Zeng, *J. Am. Chem. Soc.* **2002**, *124*, 8204–8205;

d) T. Sakaguchi, J. G. Burgess, T. Matsunaga, *Nature* **1993**, *365*, 47–49; e) J. L. Kirschvink, A. Kobayashi-Kirschvink, B. J. Woodford, *Proc. Nat. Acad. Sci.* **1992**, *89*, 7683–7687.
[3] J. E. Katz, X. Zhang, K. Attenkofer, K. W. Chapman, C. Frandsen, P. Zarzycki, K. M. Rosso, R. W. Falcone, G. A. Waychunas, B. Gilbert, *Science* **2012**, *337*, 1200–1203.
[4] a) G. C. Lavorato, A. A. de Almeida, C. Vericat, M. H. Fonticelli, *Nanotechnology* **2023**, *34*, 192001; b) H. Dong, W. Du, J. Dong, R. Che, F. Kong, W. Cheng, M. Ma, N. Gu, Y. Zhang, *Nat. Commun.* **2022**, *13*, 5365; c) G. Wang, Y. Yang, D. Han, Y. Li, *Nano Today* **2017**, *13*, 23–39; d) J. Noh, O. I. Osman, S. G. Aziz, P. Winget, J.-L. Brédas, *Sci. Technol. Adv. Mater.* **2014**, *15*, 044202.
[5] a) R. Frison, G. Cernuto, A. Cervellino, O. Zaharko, G. M. Colonna, A. Guagliardi, N. Masciocchi, *Chem. Mater.* **2013**, *25*, 4820–4827; b) F. Bourgeois, P. Gergaud, H. Renevier, C. Leclere, G. Feuillet, *J. Appl. Phys.* **2013**, *113*, 013510; c) R. L. Rebodos, P. J. Vikesland, *Langmuir* **2010**, *26*, 16745–16753.
[6] K. J. Gallagher, W. Feitknecht, U. Mannweiler, *Nature* **1968**, *217*, 1118–1121.
[7] a) P. S. Sidhu, R. J. Gilkes, A. M. Posner, *J. Inorg. Nucl. Chem.* **1977**, *39*, 1953–1958; b) K. Yuan, S. S. Lee, W. Cha, A. Ulvestad, H. Kim, B. Abdilla, N. C. Sturchio, P. Fenter, *Nat. Commun.* **2019**, *10*, 703.
[8] a) H. Cheng, C. Wang, Z. Lyu, Z. Zhu, Y. Xia, *J. Am. Chem. Soc.* **2023**, *145*, 1216–1226; b) F. Muhammad, F. Huang, Y. Cheng, X. Chen, Q. Wang, C. Zhu, Y. Zhang, X. Yang, P. Wang, H. Wei, *ACS Nano* **2022**, *16*, 20567–20576; c) Y. Zhu, X. Zhang, K. Koh, L. Kovarik, J. L. Fulton, K. M. Rosso, O. Y. Gutiérrez, *Nat. Commun.* **2020**, *11*, 3269; d) X. Pan, Y.-J. Xu, *J. Phys. Chem. C* **2013**, *117*, 17996–18005; e) M. H. Oh, T. Yu, S.-H. Yu, B. Lim, K.-T. Ko, M.-G. Willinger, D.-H. Seo, B. H. Kim, M. G. Cho, J.-H. Park, K. Kang, Y.-E. Sung, N. Pinna, T. Hyeon, *Science* **2013**, *340*, 964–968; f) S. M. Kim, M. Jeon, K. W. Kim, J. Park, I. S. Lee, *J. Am. Chem. Soc.* **2013**, *135*, 15714–15717; g) G. Xi, J. Ye, Q. Ma, N. Su, H. Bai, C. Wang, *J. Am. Chem. Soc.* **2012**, *134*, 6508–6511.
[9] a) C. Zhang, X. Wang, J. Du, Z. Gu, Y. Zhao, *Adv. Sci.* **2021**, *8*, 2002797; b) N. Singh, S. K. NaveenKumar, M. Geethika, G. Mugesh, *Angew. Chem. Int. Ed.* **2021**, *60*, 3121–3130; c) X. Mu, J. Wang, Y. Li, F. Xu, W. Long, L. Ouyang, H. Liu, Y. Jing, J. Wang, H. Dai, Q. Liu, Y. Sun, C. Liu, X.-D. Zhang, *ACS Nano* **2019**, *13*, 1870–1884; d) H. Wei, E. Wang, *Chem. Soc. Rev.* **2013**, *42*, 6060–6093.
[10] J. Liu, Z. Sun, Y. Deng, Y. Zou, C. Li, X. Guo, L. Xiong, Y. Gao, F. Li, D. Zhao, *Angew. Chem. Int. Ed.* **2009**, *48*, 5875–5879.
[11] a) J. A. Cuenca, K. Bugler, S. Taylor, D. Morgan, P. Williams, J. Bauer, A. Porch, *J. Phys. Condens. Matter* **2016**, *28*, 106002; b) W. Kim, C.-Y. Suh, S.-W. Cho, K.-M. Roh, H. Kwon, K. Song, I.-J. Shon, *Talanta* **2012**, *94*, 348–352; c) I. Kinebuchi, A. Kyono, *J. Mineral. Petrol. Sci.* **2021**, *116*, 211–219.
[12] a) A. P. Grosvenor, B. A. Kobe, M. C. Biesinger, N. S. McIntyre, *Surf. Interface Anal.* **2004**, *36*, 1564–1574; b) A. F. White, M. L. Peterson, M. F. Hochella, *Geochim. Cosmochim. Acta* **1994**, *58*, 1859–1875.
[13] a) S. P. Schwaminger, D. Bauer, P. Fraga-García, F. E. Wagner, S. Berensmeier, *CrystEngComm.* **2017**, *19*, 246–255; b) J. M. Byrne, N. Klueglein, C. Pearce, K. M. Rosso, E. Appel, A. Kappler, *Science* **2015**, *347*, 1473–1476; c) D. E. Latta, C. A. Gorski, M. I. Boyanov, E. J. O'Loughlin, K. M. Kemner, M. M. Scherer, *Environ. Sci. Technol.* **2012**, *46*, 778–786; d) C. A. Gorski, M. M. Scherer, *Environ. Sci. Technol.* **2009**, *43*, 3675–3680; e) T. C. Robinson, D. E. Latta, J. Leddy, M. M. Scherer, *Environ. Sci. Technol.* **2022**, *56*, 17454–17461.
[14] a) Y. Zhang, Z. Wang, X. Li, L. Wang, M. Yin, L. Wang, N. Chen, C. Fan, H. Song, *Adv. Mater.* **2016**, *28*, 1387–1393; b) J. Mu, C. Li, Y. Shi, G. Liu, J. Zou, D.-Y. Zhang, C. Jiang, X. Wang, L. He, P. Huang, Y. Yin, X. Chen, *Nat. Commun.* **2022**, *13*, 2513; c) B. Li, Q. Zhang, J. Cheng, Y. Feng, L. Jiang, X. Zhao, Y. Lv, K. Yang, J. Shi, W. Wei, P. Guo, J. Wang, M. Cao, W. Ding, J. Wang, D. Su, Y. Zhou, R. Gao, *ACS Nano* **2024**, *18*, 21061–21076; d) K. K. Karthik, B. V. Cheriyan, S. Rajeshkumar, M. Gopalakrishnan, *Biomed. Tech.* **2024**, *6*, 61–74; e) S. Hu, L. Wang, J. Li, D. Li, H. Zeng, T. Chen, L. Li, X. Xiang, *ACS Biomater. Sci. Eng.* **2023**, *9*, 5332–5346.
[15] a) W. Li, Z. Liu, C. Liu, Y. Guan, J. Ren, X. Qu, *Angew. Chem. Int. Ed.* **2017**, *56*, 13661–13665; b) J. Li, W. Liu, X. Wu, X. Gao, *Biomaterials* **2015**, *48*, 37–44.

Manuscript received: September 30, 2024
Accepted manuscript online: December 23, 2024
Version of record online: January 7, 2025